

Calibration of Ray-Tracing With Diffuse Scattering Against 28-GHz Directional Urban Channel Measurements

Romain Charbonnier^{ID}, Chiehpung Lai, Thierry Tenoux, Derek Caudill^{ID}, Grégory Gougeon^{ID}, Jelena Senic^{ID}, Camillo Gentile^{ID}, Member, IEEE, Yoann Corre^{ID}, Member, IEEE, Jack Chuang^{ID}, and Nada Golmie, Senior Member, IEEE

Abstract—This paper describes the calibration of the *Volcano* ray-tracing engine against channel measurements collected in an urban environment with a state-of-the-art 28-GHz directional channel sounder. A discrete set of rays, representing planar wavefronts propagating between the transmitter and receiver, were extracted from the measurements and characterized in path gain, delay, and 3D angle-of-arrival through super-resolution techniques, with average errors of only 1.2 dB, 0.55 ns, and 2.05° respectively. The extracted rays were then tracked over space as the receiver, mounted on a mobile rover equipped with military-grade GPS, traversed 66 m while amassing a total of 488 channel acquisitions. The tracked rays were then mapped to rays predicted from ray-tracing, originating through specular reflection or diffuse scattering from ambient objects. The mapping enabled object-specific calibration, namely calibrating distinct diffuse-scattering models for buildings, vehicles, and foliage. To our knowledge, this is the first effort to calibrate ray-tracing with object-specific diffuse scattering models against rays individually mapped in the path gain, delay, angle, and space domains. Results, in terms of calibrated ray-tracing parameters, fit-error statistics, and lessons learned, are included. Our chief finding was that, while most papers on millimeter-wave ray-tracing do not even consider diffuse scattering, it accounted for 20% of the total received power, whereas diffraction accounted for less than 1%.

Index Terms—5G, millimeter-wave, mmWave, tuning, channel sounder, channel model.

I. INTRODUCTION

RAUDIO-FREQUENCY channel models define the physical medium through which communications signals

Manuscript received April 10, 2020; revised September 3, 2020 and October 14, 2020; accepted November 8, 2020. Date of publication November 18, 2020; date of current version January 22, 2021. This work was supported by the Publication of the United States government, not subject to copyright in the U.S. The review of this article was coordinated by Dr. L. Dai. (*Correspondence author: Camillo Gentile*).

Romain Charbonnier, Thierry Tenoux, Grégory Gougeon, and Yoann Corre are with the Siradel, 3, Allée Adolphe Bobitre - CS 24 343 - 35043, Rennes Cedex - France (e-mail: rcharbonnier@siradel.com; ttenoux@siradel.com; ggougeon@siradel.com; ycorre@siradel.com).

Chiehpung Lai, Jelena Senic, Camillo Gentile, Jack Chuang, and Nada Golmie are with the Wireless Networks Division, National Institute of Standards and Technology, Gaithersburg, MD 20899 USA (e-mail: chiehpung.lai@nist.gov; jelena.senic@nist.gov; camillo.gentile@nist.gov; jack.chuang@nist.gov; nada.golmie@nist.gov).

Derek Caudill is with the RF Technology Division, National Institute of Standards and Technology, Boulder, CO 80305 USA (e-mail: derek.caudill@nist.gov).

Digital Object Identifier 10.1109/TVT.2020.3038620

propagate, thus are essential to the analysis, design, and deployment of wireless networks. The most widely used channel models to date are empirical [1]–[23], i.e., their large-scale metrics (path-loss exponent, RMS delay and angle spreads, Ricean K-factor, etc.) are derived from measurements only; although their predictions can be accurate in environment(s) supported by measurement data, they often do not generalize well to other environments [24]. Consequently, the scientific and industrial communities have been migrating to deterministic models, in which the channel is represented as a discrete set of planar wavefronts,¹ or *rays*, propagating between the transmitter and receiver. The properties of the rays – path gain, delay, angle-of-departure (AoD), and angle-of-arrival (AoA) – can be predicted through *ray-tracing*, provided a GIS (Geometric Information System) database to represent the environment; since the environment is represented geometrically, predictions are more generalizable than empirical models. Widespread use of ray-tracing, once prohibitively expensive, has been facilitated by advances in computational methods and resources over the past decade.

Given the recent interest in 5G cellular at 26, 28, 38, and 42 GHz bands, as well as the unlicensed 60-GHz band for dense wireless backhaul in urban and suburban environments, more and more papers generate channel metrics and network performance for millimeter-wave (mmWave) communications through ray-tracing [25]–[53]. This is in part because ray-tracing is more efficient at such high frequencies since diffraction, which is the most computationally expensive propagation mechanism, becomes negligible due to the narrowing of the Fresnel zone – so waves behave like light. This gives way to direct transmission as the dominant mechanism in line-of-sight (LOS) conditions, and specular reflection in non-LOS since the direct ray will suffer much greater penetration and diffraction losses than at sub-6-GHz [54]. What is more relevant at mmWave is *diffuse scattering* due to the fact that the roughness of object surfaces (e.g., buildings, vehicles) can be comparable to the signal wavelength and so objects appear electrically large, as do the intricacies of foliage and other typical clutter. In fact, it

¹The planar wavefront assumption is valid so long as receiver is in the far field (10-20 wavelengths, e.g. > 21 cm at 28 GHz) of the transmitter and any ambient scatterers.

has been demonstrated that diffuse scattering can account for up to 40% of the total received power at mmWave [55]–[56]. Despite the importance of diffuse scattering at mmWave, only [28], [47]–[53] even consider it out of the ray-tracing papers cited above.

Although ray-tracing is more generalizable than empirical channel models, its prediction accuracy nevertheless hinges upon measurements for the purpose of tuning (a.k.a. *calibrating*) its parameters, such as the material characteristics of surrounding objects. Because cellular technology to date (1G–4G) has operated exclusively in the sub-6-GHz band, there is a wealth of channel measurements to support the reliable tuning of ray-tracing parameters across many frequency bands, environments, and materials types; on the contrary, since 5G is still in its advent, measurements at mmWave are still lacking. As a result, many papers on mmWave ray-tracing neither calibrate its parameters nor validate the results it produces [25]–[28].

In terms of validation, some papers draw comparisons to published large-scale channel metrics [29]–[34]. Other papers compare results against actual measurements, however the match is often poor because the parameters are based on, or extrapolated from, sub-6-GHz measurements [35]. Measurement comparisons are most commonly evaluated through *aggregate statistics* – statistics on the fit error between measured path loss [36]–[40] or measured RMS delay or angle spreads [35], [41]–[42] and the respective metric given from the *sum* over predicted rays. The drawback of aggregate statistics is that the fit error per ray may still be large, hence comparisons employing *individual statistics* – statistics on the fit error between rays extracted individually from the measurements and corresponding predicted rays – are more reliable: in [43], the comparison is based on the delay and angle of individual rays, whereas in [44] path gain is also taken into account.

More relevant to our work are papers – there are just a few – that go beyond validation and actually tune parameters against measurements. These papers closely follow the various tiers of validation discussed above: In [45], calibration is based on path loss alone whereas in [46] it is also based on RMS delay spread, both employing aggregate statistics. Calibration through individual statistics is much more challenging – it necessitates mapping measured rays to predicted rays incident on ambient objects – however, once obtained, the mapping enables object-specific parameter tuning: in [47]–[48], the mapping is performed only in the delay domain of the rays; in [49]–[52], the mapping is extended to the space domain, over which the measured rays are tracked as the receiver moves around the environment.

An alternative calibration approach adopted in [53] is to precisely characterize – in a controlled manner within an anechoic chamber – the material characteristics of discrete objects typically found in an environment, bypassing the need to collect data in the field and map objects *a posteriori*. However, the outdoor environment, for example, is composed from hundreds of objects with a wide range of materials – a building façade alone is a complex composite of concrete, metal, and glass with

different thickness and roughness – so this approach has limited application.

To our knowledge, only [53] accounts for the angle domain in tuning. The importance of the angle domain for calibration cannot be overstated for the following three reasons:

- 1) mmWave systems will incorporate highly directional antennas (because they have high gain) to recover from the greater path loss experienced at these frequencies, so accurate directional channels are essential to support the design of these systems;
- 2) Diffuse rays tend to cluster around specular rays in the delay and angle domains [51], [55]–[57], so angle information is critical to the accurate characterization of diffuse scattering;
- 3) Material characteristics (e.g., reflection loss of the Fresnel equations) are angle dependent.

While ray-tracing, in theory, is well suited for the mmWave regime, its suitability has not neither been thoroughly investigated nor confirmed due to lack of precision measurements to date. The intention of this paper is to help fill that void. To that end, in a joint collaboration, we calibrate the parameters of Siradel's *Volcano*² ray-tracer [58] against measurements collected by the National Institute of Standards and Technology in an urban environment at 28 GHz. The three main contributions of our work are as follows:

- 1) High-precision measurements with our state-of-the-art directional channel sounder, collected as the receiver, mounted on a mobile rover equipped with military-grade GPS, traversed 66 m while amassing a total 488 channel acquisitions. From each acquisition, rays were extracted in path gain, delay, and 3D AoA through super-resolution techniques, yielding average extraction errors of only 1.2 dB, 0.55 ns, and 2.05° respectively;
- 2) A calibration methodology based on tracking the extracted rays as the receiver moved in space, and subsequently mapping – through individual statistics on the fit error–measured rays to rays predicted from ray-tracing;
- 3) Object-specific calibration of diffuse scattering models – namely distinct models for buildings, vehicles, and foliage – made possible through the mapping obtained.

The remainder of this paper is developed as follows: Section II describes our channel sounder and extensive measurement campaign; Section III describes our *Volcano* ray-tracer, including diffuse scattering models for buildings, vehicles, and foliage; Section IV describes the methodology implemented for tuning the ray-tracer against the measurements collected; Section V presents the statistics on the fit error and the lessons learned from the calibration process; the last section is reserved for conclusions.

²Certain commercial equipment, instruments, or materials are identified in this paper in order to specify the experimental procedure adequately. Such identification is not intended to imply recommendation or endorsement by the National Institute of Standards and Technology, nor is it intended to imply that the materials or equipment identified are necessarily the best available for the purpose.



Fig. 1. (a) NIST 28-GHz switched-array channel sounder. The inset of the Rx array shows more detail. (b) Data collection environment in downtown Boulder, Colorado.

II. CHANNEL MEASUREMENTS

A. Measurement System

Fig. 1(a) displays the NIST 28-GHz switched-array channel sounder [59],³ used for data collection. The transmitter (Tx) featured a single dipole antenna with omni-directional pattern in azimuth (AZ) and 30° beamwidth in elevation (EL), and 2 dBi boresight gain. The receiver (Rx) featured a circular array of 16 horn antennas (see inset in Fig. 1(a)), each with 45° AZ and EL beamwidth, and 16.6 dBi boresight gain. To avoid “blind spots,” the angular spacing between antennas was matched to the beamwidth of the horns; specifically, the antennas were spaced at 45° in AZ; in EL, adjacent antennas were alternately pointed outwards at 0° and upwards at 45° towards the Tx; the resulting array constellation provided 360° AZ field-of-view (FoV) and 90° EL FoV (-22.5° to 67.5°). The 3D constellation enabled characterizing AoA in both AZ and EL.

The system generated a repeating 32767-bit Pseudorandom Noise (PN) codeword that had a chip rate of 1 GHz (1-ns delay resolution). The codeword was generated at 2.5 GHz intermediate frequency (IF) and then upconverted to an RF center frequency of precisely 28.5 GHz and transmitted at 30 dBm. With 0.5 ps synchronization provided through Rubidium clocks, the signal was transmitted continuously while the received signal was sequentially switched through the Rx antennas every two codewords.⁴ Thus, a channel acquisition consisted of a full sweep of the 16 Rx antennas, requiring 1.05 ms. At the Rx, the received signal was downconverted back to IF, amplified, and then digitized at 40 Gsamples/s (oversampling both reduced aliasing and improved the signal-to-noise ratio). For each antenna, the received signal was correlated with the known PN codeword to generate a complex channel impulse

response (CIR). We refer to a single *acquisition* as a set of 16 CIRs associated with the Rx array. Factoring in the Tx power, the antenna gains, the Rx noise figure, and the processing gain of the PN sequence, the maximum measurable path loss of the system was 170 dB.

B. Measurement Campaign

Field measurements were collected in downtown Boulder, Colorado during the month of July; Fig. 1(b) displays a photograph of the urban environment studied, sectioned off by Walnut, Lawry, Broadway, and 13th streets; the tallest building in the surroundings was 36.3 m high. The stationary Tx was mounted on a tripod at 2.5 m in a parking lot; the Rx was mounted on the mobile rover at 1.6 m. The rover enabled rapid and continuous collection of channel data while recording the location, velocity, and heading of the Rx array per acquisition – essential to the analysis of the data collected. This spatial information was recorded through a Differential Global Positioning System (DGPS): Before field measurements, the Tx location was surveyed for four hours to acquire its precise latitude, longitude, and altitude; during field measurements, errors in the DGPS system were monitored at the Tx and corrections were calculated in real time and sent to the rover’s GPS antenna (mounted on top of the Rx array, as shown in Fig. 1(a)) through a 900 MHz radio link. The DGPS system delivered cm-level localization accuracy.

The rover followed a linear trajectory along the sidewalk (shown in Fig. 1(b)) with an average speed of 0.35 m/s, under a canopy of trees and aligned by cars on both sides. The Tx-Rx distance ranged from 6.1 m to 66.1 m, over which 61 channel *captures* were collected, with an average of 1.1 m in between. Each *large-scale* channel capture consisted of eight *small-scale* channel acquisitions (about one wavelength apart) triggered sequentially, producing a rich data set for the accurate characterization of diffuse scattering.

³The system features reported in this citation are for our 83-GHz switched-array channel sounder, however the features of our 28-GHz switched-array channel sounder are almost identical.

⁴The second codeword was used as a buffer between switching.

C. Extraction of Measured Rays

For each acquisition, the 16 CIRs were coherently combined through the SAGE super-resolution algorithm to extract a discrete set of measured rays: Given the wide beamwidth of the Rx horns (45°), we relied chiefly on our high delay resolution (1 ns) to resolve different rays. If two rays arrived within the same delay bin and beamwidth, they could still be resolved to some extent if one of the rays was at least 6 dB weaker than the other one (rule of thumb). Our SAGE algorithm is based on time difference of arrival (TDoA): Given the wide beamwidth of the Rx horns (45°), we relied chiefly on our high delay resolution (1 ns) to resolve different rays. If two rays arrived within the same delay bin and beamwidth, they could still be resolved to some extent if one of the rays was at least 6 dB weaker than the other one (rule of thumb). Our SAGE algorithm is based on time difference of arrival (TDoA): If a ray was detected within the same delay bin by at least three adjacent Rx horns in the array, the relative difference between their delays – we oversample by 10x (at 25 ps) to get fine delay accuracy – against the relative displacement between their known phase centers (within micrometers) was used to estimate AoA. The SAGE algorithm is also based on the “power difference of arrival”: the relative difference in the detected power of the ray between the horns against the relative antenna gains along the ray’s AoA, was also incorporated to estimate AoA. Details of the algorithm are described in [60].

The ray properties were extracted in a four-dimensional domain: path gain, delay, AZ AoA, and EL AoA. Any measurement taken with the channel sounder captured not only the response of the channel, but also the response of the sounder itself, i.e., the directional patterns of the antennas and the hardware responses of the Tx and Rx front ends. Accordingly, SAGE de-embedded the antenna patterns as part of the algorithm while the responses of the Tx and Rx front ends were removed through pre-distortion filters designed from a back-to-back correction method [61]. Hence the extracted rays represented the “pristine” response of the channel itself (without the measurement system), thus were analogous to the ray-tracing predictions. Fig. 2 shows rays extracted for an illustrative location Rx11, displayed as power angle-delay profiles (PADPs) for AZ and EL. The relative path gain – relative to the strongest ray per Rx location (the direct ray in our scenario) – is displayed against the color bar.

III. VOLCANO RAY-TRACER

Ray-tracing is an efficient technique to predict channel rays and their properties through electromagnetic fields theory. Transmitted and reflected rays are predicted through the Fresnel equations [62] while diffracted rays are predicted through the Uniform Theory of Diffraction (UTD) [63]. Diffuse rays, on the other hand, are modeled as an empirical “add-on” to reflection and diffraction. The predictions require the geometry, polarization, and electromagnetic material characteristics (e.g., permittivity, permeability, conductivity, roughness) of the constituent objects of an environment. With the material characteristics in hand, the ray geometries can then be constructed.

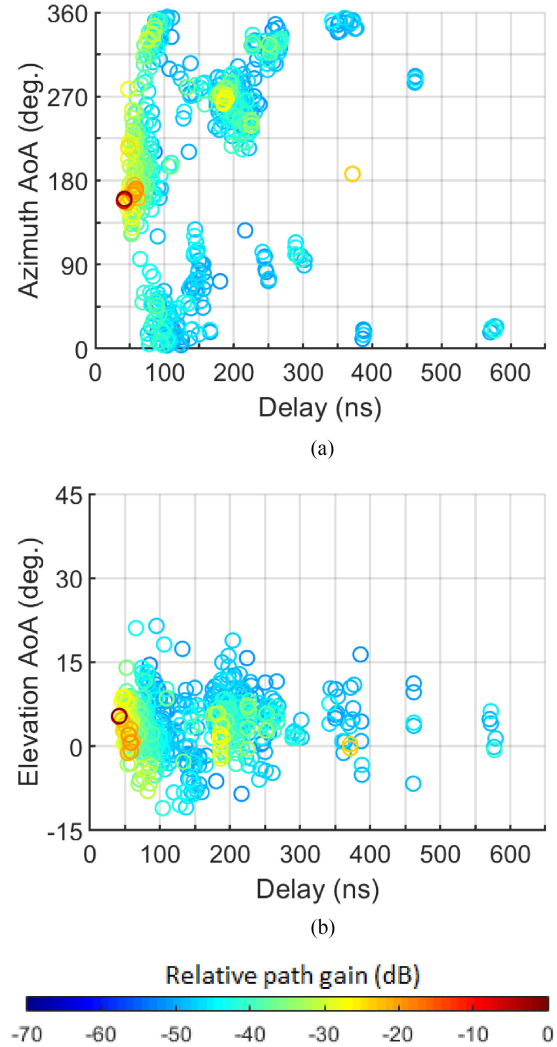


Fig. 2. Measured rays, extracted from a channel capture at illustrative location Rx11, displayed as power angle-delay profiles in (a) azimuth and (b) elevation, where the path gain is color-coded against the color bar. The dark red circle corresponds to the direct ray.

There are two main approaches to ray-tracing [62]. The first is to compute exact ray geometries between known Tx and Rx locations by enumerating all possible combinations of surface reflections and edge diffractions. The second approach, referred to as *ray-launching* (a.k.a *ray-bouncing*, *ray-shooting*), is to generate a discrete number of rays emanating from the Tx at a given angular resolution and trace the most dominant to the Rx. While the first approach provides most accurate results, the second allows for much faster point-to-point or point-to-grid predictions.

The 3D ray-tracing engine used for analysis and calibration in this study is called *Volcano* [58], engineering by the co-authors from Siradel. Since *Volcano* is geared towards radio planning and simulation of scenarios in large, complex environments with numerous nodes, it was developed based on ray-launching principles. The accuracy of the ray geometries and fields it predicts has nevertheless been demonstrated to be comparable to the exact approach [58], while reducing the computation time down

to a few seconds to a few minutes per Rx location (depending on the GIS complexity and number of allowed interactions). In the sequel, we describe how *Volcano* constructs the ray geometries for transmission, reflection, and diffraction, and describe the models for diffuse scattering.

A. Transmission, Reflection, and Diffraction

Upon launching the rays from the Tx, interactions with objects are detected for each ray and those interactions lead to splitting of the ray into a reflected sub-ray or several diffracted sub-rays in new directions. Each sub-ray is constrained to a *visibility region* (whose definition depends on the ray-launching algorithm) that contains the Rx. Propagation in the horizontal and vertical planes is managed in successive steps. First, rays are launched horizontally towards all vertical surfaces and edges; for each horizontal ray, a visibility region that determines exactly where subsequent interactions will occur (at the boundary of the visibility region) and where potential receivers are located (within the visibility region) is constructed; the horizontal rays are classified as transmitted, reflected, or diffracted each time a vertical surface or edge is met. Next, each horizontal ray gives way to analysis in the vertical plane: a virtual 2D scene is constructed as the cross-section of the 3D GIS objects in the vertical plane intersected by the horizontal rays. Additional vertical rays are launched in this virtual 2D scene, allowing for reflections on non-vertical surfaces and diffractions on non-vertical edges. Finally, the horizontal and vertical trajectories are merged to yield the composite 3D ray. High prediction fidelity is ensured thanks to ray decomposition when multiple interactions are detected within the visibility region and to *a posteriori* correction at a given Rx location.

B. Diffuse Scattering

Diffuse scattering occurs when a ray incident upon a surface whose roughness is comparable to the wavelength of the signal is scattered in random directions (as opposed to the specular direction predicted by Fresnel equations). As mentioned earlier, diffuse scattering – from small objects or from large objects with intricate geometry or permeable surfaces such as foliage – is significant in small-cell urban and suburban scenarios at mmWave, and moreover is object specific. In this subsection, we describe distinct models for buildings and vehicles, and for foliage.

1) Buildings and Vehicles: Incorporating diffuse scattering from the building façades and vehicle surfaces was decided after preliminary analysis of the measurements indicated that the predicted specular contributions were insufficient to reproduce the delay and angle spreads observed. Diffuse scattering from buildings and vehicles is modeled by *Volcano* in tandem with specular reflection [64]. Specifically, surfaces visible to the Tx and that are within the visibility region are discretized into uniform tiles, as illustrated in Fig. 3(a). The wave incident on the surface is diffused in all directions, represented as multiple rays constructed from the center of each tile, as illustrated in Fig. 3(b).

The path gain, PG_{ER} , for each diffuse ray is given through an empirically defined radiation pattern governed by the *Effective*

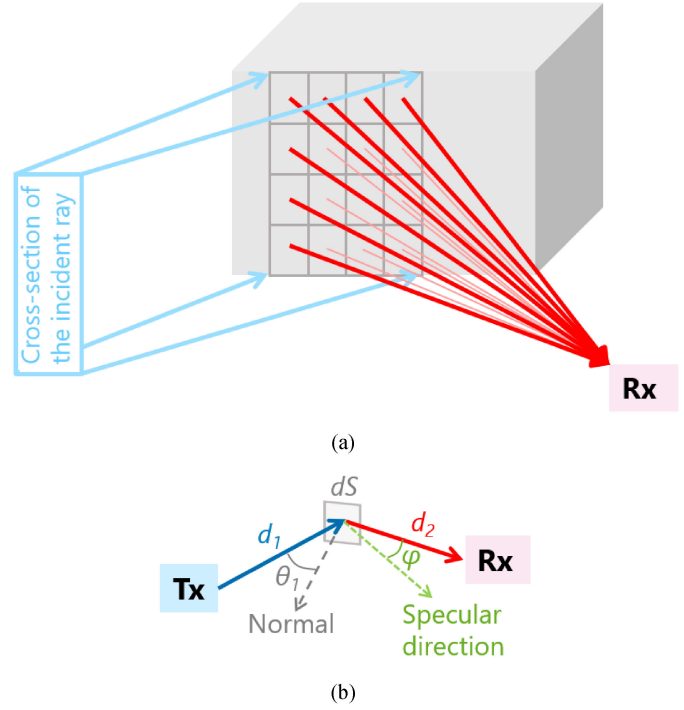


Fig. 3. Diffuse scattering model for buildings and vehicles. (a) Surface discretization into tiles. (b) Ray geometry.

Roughness (ER) model [57]:

$$PG_{ER} = S^2 \cdot \frac{\cos \theta_1 \cdot dS}{4\pi \cdot d_1^2 \cdot d_2^2} \cdot [S_0 \cdot f(\varphi)]^2$$

$$f(\varphi) = \left(\frac{1 + \cos \varphi}{2} \right)^{\alpha/2}$$

$$S_0^2 = 1 / \iint f(\varphi)^2 d^2\Omega \quad (1)$$

where S is the ratio between the total diffuse field and the incident field; dS is the tile area; d_1 and d_2 are the respective distances to and from the surface; θ_1 is the incident angle with the surface normal and φ is the angle between the specular and diffuse rays; α is a parameter that controls the directivity of the diffuse radiation pattern.

2) Foliage: Before extending it to mmWave, *Volcano* implemented two types of interaction with foliage – top diffraction and transmission – but not scattering. The 28-GHz measurements, however, revealed that besides from buildings and vehicles, diffuse scattering from foliage – notably from large trees in the environment – caused dispersion in both horizontal and vertical directions. In turn, the behavior was incorporated to deliver enhanced precision.

A tree is represented as a rectanguloid with finite dimensions, partitioned into a discrete number of cubic voxels with ρ particles per unit volume, as depicted in Fig. 4(a). The model generates diffuse rays with varying delays, AoDs, and AoAs, as depicted in Fig. 4(b). The path gain, PG_{FOL} , resulting from scattering of the incident wave with the foliage is decomposed into a direct

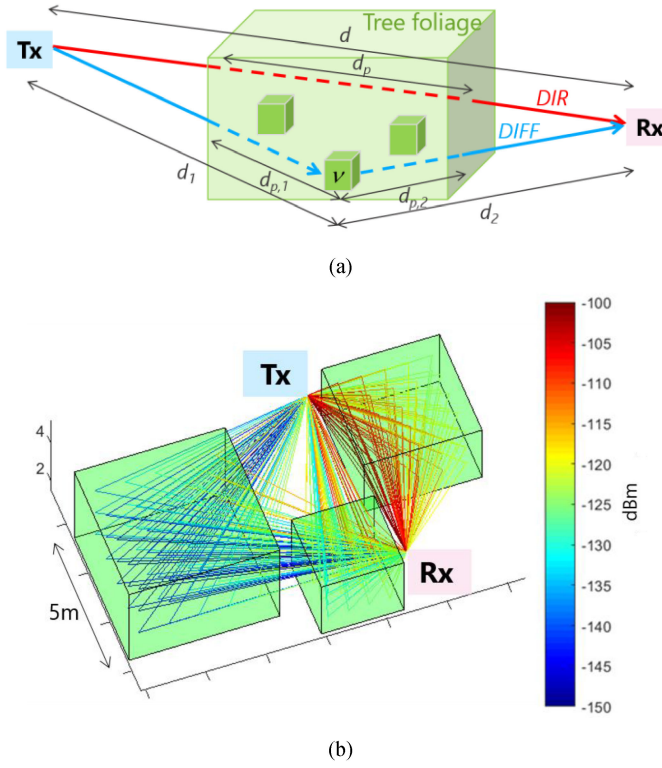


Fig. 4. Diffuse scattering model for foliage. (a) Volume discretization into voxels. (b) Ray geometry for multiple trees.

ray (PG_{DIR}) plus numerous diffuse rays (PG_{DIFF}) :

$$PG_{FOL} = PG_{DIR} + PG_{DIFF}$$

$$PG_{DIR} = \left(\frac{\lambda}{4\pi} \right)^2 \frac{e^{-\kappa_e d_p}}{d^2}$$

$$PG_{DIFF} = \left(\frac{\lambda}{4\pi} \right)^2 \int_V \frac{e^{-\kappa_e [d_{P,1}(v) + d_{P,2}(v)]}}{d_1^2(v) d_2^2(v)} \frac{\sigma_{bi}(v)}{4\pi} dv \quad (2)$$

The expression for PG_{DIR} is given from the free-space loss over d reduced by scattering loss along the cross-section of the tree, d_p ; the scattering loss is characterized by the extinction coefficient $\kappa_e = \rho \cdot \sigma_e$, where σ_e (m^2) is the average extinction cross-section [65]. The expression for PG_{DIFF} is derived from a bi-static radar equation [65], integrating all voxels in the volume V .⁵ The integrand is similar to PG_{DIR} in terms of free-space loss, but the distances $d_{P,i}$ and d_i account for the incident direction ($i = 1$) and the scattered direction ($i = 2$), and the path gain is scaled by the bi-static scattering cross-section, $\sigma_{bi}(v)$ (m^2):

$$\sigma_{bi}(v) = \sigma_s \cdot p[\phi(v)]$$

$$p(\phi) = \alpha \cdot f(\phi) + (1 - \gamma)$$

$$f(\phi) = \left(\frac{2}{\beta_s} \right)^2 e^{-\left(\frac{\phi}{\beta_s} \right)^2} \quad (3)$$

⁵As a first-order approximation, interaction between multiple voxels is neglected.

The bi-static scattering cross-section is proportional to the total scattering cross-section, σ_s (m^2), modulated by the scattering pattern, $p(\phi)$, where $\phi(v)$ is the horizontal angle between the incident and scattered waves at voxel v ; σ_s is related to σ_e through the albedo, $\omega = \sigma_s / \sigma_e$. The scattering pattern $p(\phi)$ was adopted from [66] and is defined by the effective beamwidth, β_s (deg.), of the forward lobe centered on the incident direction ($\phi(v) = 0$) and an isotropic ground level, γ , as observed from the measurements.

IV. CALIBRATION PROCESS

In the extension of *Volcano* from microwave to mmWave, many challenges were encountered and subsequently solved while reconciling theory with actual channel measurements, driving the ray-tracing settings and the calibration process described in this section. While the measurement data was collected in a particular environment, the building, vehicle, and foliage models calibrated from the data can be applied to any urban environment, so long as the GIS database of that urban environment, containing these three object types, is available.

A. Ray-Tracing Settings and Initial Parameters

The Fresnel zone is narrower at mmWave than at microwave, hence the penetration losses of rays from objects in close proximity may be substantially different from each other; therefore rays must be traced individually, translating into more stringent requirements on the GIS resolution. The GIS database used for ray-tracing downtown Boulder was obtained from OpenStreetMap [67], which furnishes 2D vectors of buildings with precision on the order of 1-2 meters, sufficient to accurately represent buildings and other ambient structures that were likely to attenuate, reflect, or diffract rays. The building heights were estimated from the number of floors. Fig. 5(a) illustrates the 3D database for the environment, with the buildings labeled. The red line delineates the trajectory of the Rx during the 61 channel captures, surrounded by 3D models for cars (grey boxes) and trees (green boxes). The 3D model for the surrounding cars, depicted in Fig. 5(b), was placed in the area according to the numerous photographs and videos recorded during the campaign. The 3D tree model was inserted based on GoogleEarth 3D views [68], with trunk heights (around 1.8 m) and crown heights (7–8 meters) also according to the photographs and videos.

The output from the ray-tracer was a discrete set of predicted rays characterized in the same four-dimensional property domain as the rays extracted from the acquisitions (path gain, delay, AZ AoA, and EL AoA). The predicted specular rays from the buildings are depicted in Fig. 5(a) for location Rx11 (red square) and their path gain color-coded against the color bar. For the sake of computational efficiency, the prediction was configured with a maximum of two specular reflections and one diffraction per ray. With diffuse scattering activated, the number of predicted rays could easily fall into the hundreds, dependent on the tile resolution of the building and vehicle models and the voxel resolution of the foliage model. To strike a balance between computational efficiency and accuracy, the ray resolution was set to 5 ns in delay, 5° in AZ, and 2° in EL.

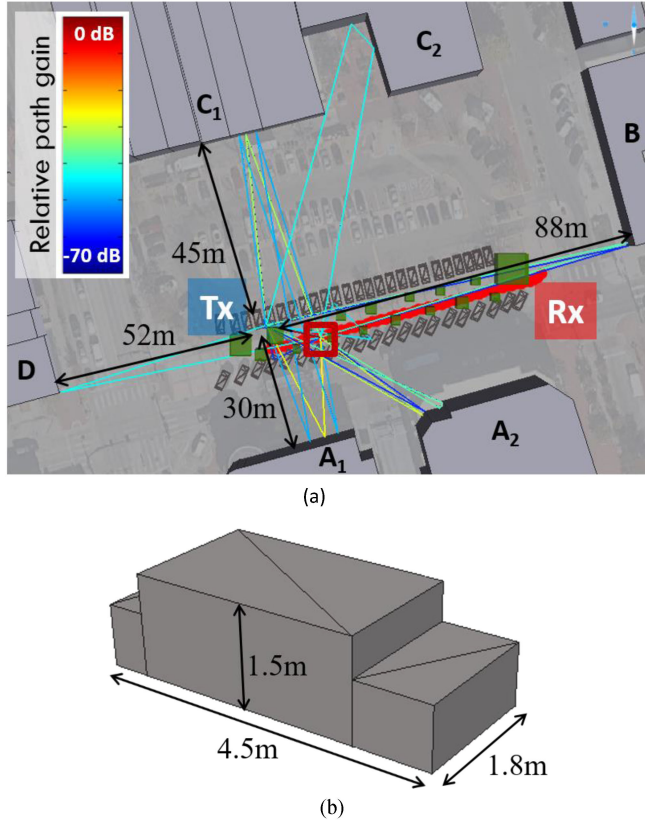


Fig. 5. Geometric database for buildings (labeled A-D), cars (grey boxes), and trees (green boxes) in the measurement environment in downtown Boulder. (a) Tx and 61 Rx locations in the measurement campaign; superimposed are predicted specular rays (up to 2_{nd} order) from the buildings for illustrative location Rx11 (red square); the rays are color-coded against path gain. (b) 3D vehicle model.

Table I contains a comprehensive set of initial ray-tracing parameters, mostly provided through ITU recommendations. The building dielectric characteristics were obtained from the concrete characteristics in [69] and the S and α parameters of the ER scattering model in (1) for buildings and vehicles were derived empirically from measurements at sub-6 GHz [57]. The foliage scattering parameters in (2) and (3) were obtained from the “London platane” description in [60]. The atmospheric gas absorption at 28 GHz [71] was added to the free-space loss.

B. Calibration Methodology

The goal of the calibration process was to refine the initial parameters in order to minimize the fit error between the measured and predicted rays in the four-dimensional domain; the underlying assumption was that a correct mapping from the measured rays to the predicted rays was obtained. Obtaining the mapping was challenging since the individual propagation mechanisms (transmission, specular reflection, diffraction, and diffuse scattering), when combined into a sole prediction, have many input parameters and an output that is a complex product of their cross correlations. To render the calibration process tractable, it was broken down into two steps:

TABLE I
RAY-TRACING PARAMETERS

Parameters	Initial	Intermediate	Final
Building	Permittivity	$5.31 - j0.32$	$5.31 - j0.32$
	Spec. scaling factor	1	0.8
	S	N/A	0.35
	α	N/A	3
	Diff. scaling factor	N/A	1
Vehicle	Permittivity	∞	∞
	Spec. scaling factor	1	0
	S	N/A	0.35
	α	N/A	3
	Diff. scaling factor	N/A	1
Foliage	κ_e	N/A	0.441 Np/m
	β_s	N/A	18°
	γ	N/A	0.95
	ω	N/A	0.95
	Diff. scaling factor	N/A	1

1) *Obtain Mapping From Measured Rays to Predicted Rays:* Fig. 6(a) displays the AZ and EL PADPs for the measured rays, for illustrative location Rx11 as well as across all Rx locations combined. To obtain the mapping, rays were first predicted using the initial parameters. The mapping was facilitated by deactivating diffuse scattering to reduce ray clutter, leaving only transmitted, reflected, and diffracted rays. In addition, predicted rays whose AoA fell outside the channel sounder’s Rx FoV were discarded. We refer to this as the *initial* calibration stage and the resultant predicted PADPs are shown in Fig. 6(b). The predictions revealed rays with distinct properties in the four-dimensional domain, enabling reliable mapping through careful visual inspection per Rx location, as well as through signature *tracks* of rays formed over all Rx’s. Tracks that were clearly mapped between the measured and predicted PADPs are evidenced in Fig. 7, namely tracks of the direct ray between the Tx and Rx and of first-order reflections from the buildings. Although there was measurement error as well as prediction error (due to the inaccuracies in the GIS database) in the ray properties per Rx location, a reliable mapping was nevertheless obtained thanks to: 1. the four-dimensional property domain, each dimension adding enhanced resolution capability to discriminate between individual rays; 2. the mapping between tracks of rays, so the error per Rx location tended to average out over all Rx’s.

Since the direct ray generates no scattering, no measured diffuse rays were clustered with it. Also, measured diffracted rays were too weak to recognize and so were not considered further. What remained among the measured rays were the mapped rays and the rays unmapped altogether. Accordingly, the unmapped rays were dismissed as diffuse and subsequently clustered with the mapped rays. The resultant clusters were

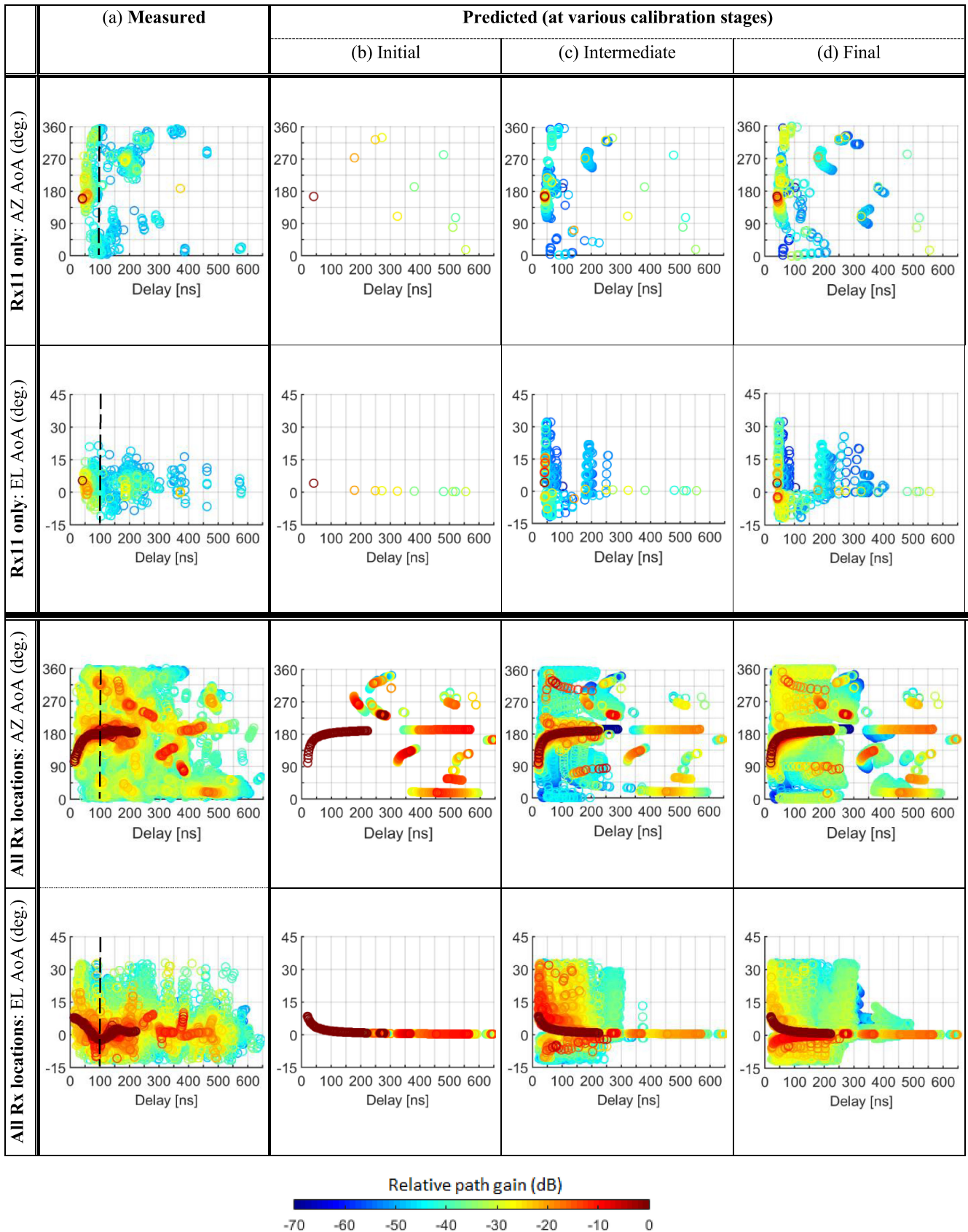


Fig. 6. Azimuth and elevation power angle-delay profiles for illustrative location Rx11 and for all Rx locations combined. The profiles are shown for (a) the measured rays and for the predicted rays in their various stages of calibration: (b) Initial – specular rays using initial ray-tracing parameters (c) Intermediate – calibrated specular rays and diffuse rays using initial parameters (d) Final – calibrated specular rays and diffuse rays.

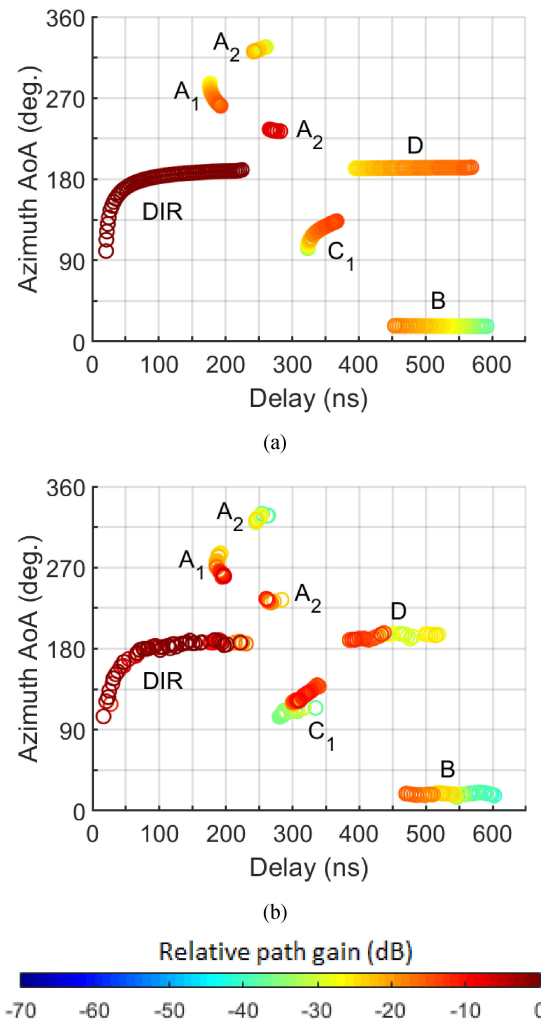


Fig. 7. Tracks of rays (across all Rx locations) that were clearly mapped between the measured and predicted PADPs are evidenced, namely tracks of the direct ray (DIR) between the Tx and Rx and of first-order reflections from the buildings (labeled in reference to Fig. 5(a)). (a) Predicted tracks from the initial parameters. (b) Measured tracks.

classified as originating either from a building, a vehicle, or foliage in the following manner: Clusters with delay in excess of 100 ns and featuring a strong specular component that followed the signature tracks in Fig. 7 could clearly be mapped to buildings. Because these clusters had narrow angular spread (a few degrees), they were sufficiently separated in the angle-delay domains for unambiguous clustering, with few exceptions of overlapping rays between clusters per Rx location. This was not the case for clusters arriving with delay less than 100 ns (demarcated in Fig. 6(a) with a vertical dotted line), originating either from vehicles or foliage, given their proximity to the Rx's; in those cases, EL AoA was used to discriminate between the two cluster classes – unmapped rays with positive elevation AoA were dismissed as from foliage and those with negative AoA as from vehicles – and subsequently clustered with the closest mapped rays.

Due to the limited EL FoV of the Rx array (-22.5° to 67.5°), ground rays at Rx locations close to the Tx could not be detected,

i.e., for ground reflections with EL AoA less than -22.5° ; for Rx locations far from the Tx, the delay difference between the direct ray and ground rays was less than the 1-ns resolution of the system; for Rx locations in between (Rx8-Rx27), the ground rays were mostly obstructed by vehicles and tree trunks. As such, we could not detect enough ground rays to develop a reliable model for ground reflection and scattering.

2) Calibrate Ray-Tracing Parameters Based on Mapping Obtained: Once the mapping was obtained, the predicted rays were calibrated against the measured rays. First, the specular model parameters were calibrated through an exhaustive search based on individual statistics, namely to minimize the mean error (mean across all the Rx's) in path gain between the mapped measured and predicted specular rays per Rx location. Then, the diffuse scattering models described in Section III – building, vehicle, or foliage depending on the mapping obtained – were activated with their initial parameters. We refer to this as the *intermediate* calibration stage and the resultant PADPs are shown in Fig. 6(c). For the diffuse rays, a reliable mapping was unrealistic given the sheer number of rays and the randomness of their path gain, delay, and angle. Instead, six large-scale channel metrics – namely the mean and RMS spread of the delay, AZ AoA, and EL AoA – were employed to calibrate the parameters of the scattering models through aggregate statistics. Specifically, these parameters were calibrated through an exhaustive search in order to minimize the mean errors (mean across all Rx's) between the metrics for all measured rays and the metrics for all predicted rays per Rx location. More on the errors are presented in the following section. We refer to this as the *final* calibration stage and the resultant PADPs are shown in Fig. 6(d).

V. OBSERVATIONS AND RESULTS

All parameters that resulted from the intermediate and final calibrations are listed in Table I – alongside the initial parameters – with modifications highlighted in red.

Direct ray: The predicted delay, AZ AoA, and EL AoA of the direct ray were given directly from the geometry between the Tx and Rx and the predicted path gain of the direct ray by mapping its delay through Friis transmission. These properties could then be considered as ground-truth against which the measured properties of the direct ray were compared, in order to estimate the measurement error of our channel sounder. Accordingly, the average / standard deviation of the measurement error compiled across all Rx's was 1.2 dB / 1.76 dB in path gain, 0.55 ns / 1.08 ns in delay, 2.8° / 2.3° in AZ AoA, and 1.3° / 1.5° in EL AoA.

Specular rays: As evidenced in Fig. 7, a good match was also observed for the first-order building reflections; the effect of calibration was to reduce path gain on average by the *specular scaling factor* of 0.8. Specular reflections and diffractions from the vehicles, on the other hand, were deactivated (specular scaling factor = 0) because, upon inspection, the strong rays predicted did not correlate with the measurements; this most likely stemmed from discrepancies in the generic vehicle model used to represent all ambient vehicles and in the placement of the model throughout the area.

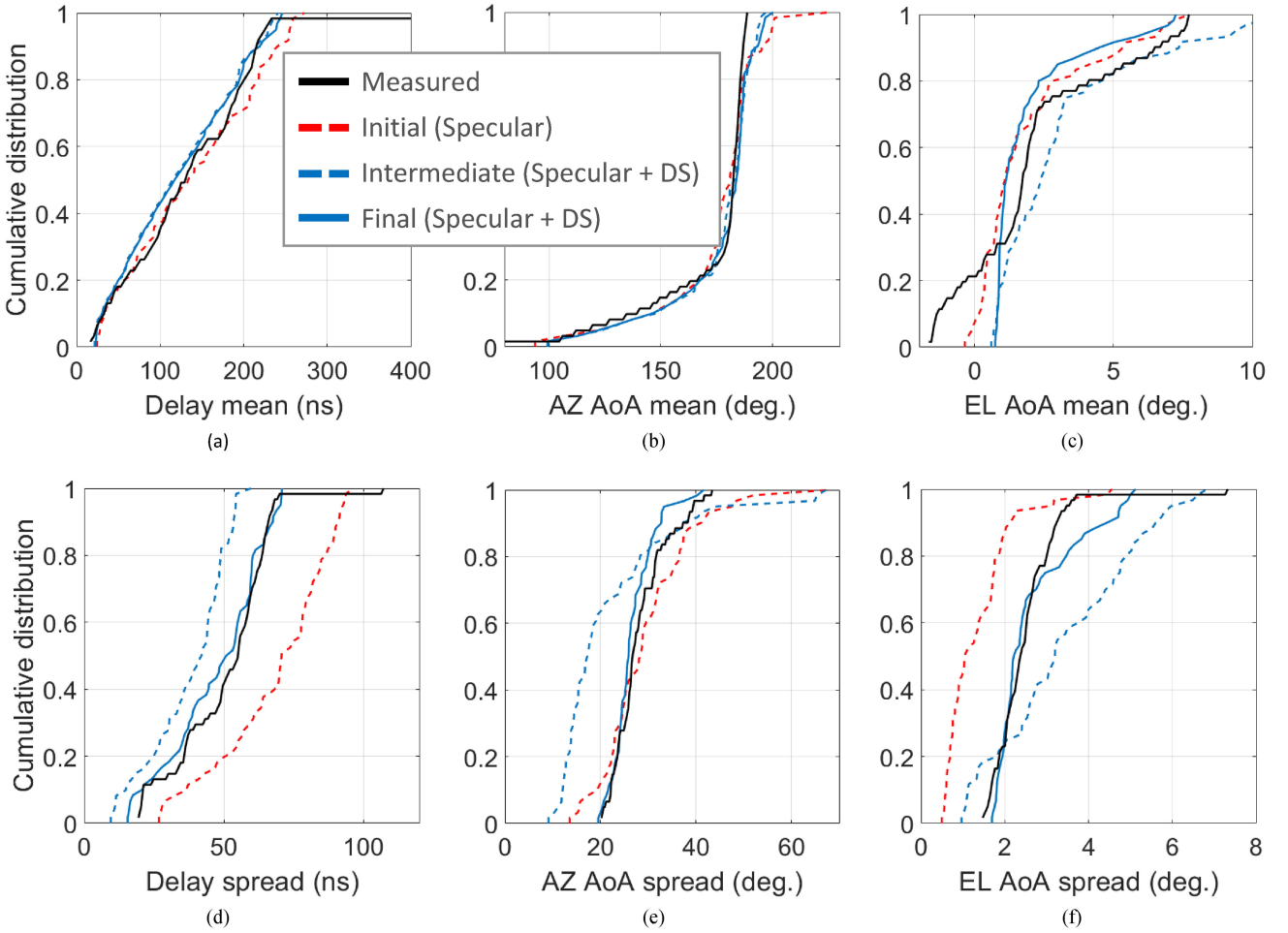


Fig. 8. Cumulative Distribution Function (CDF) of large-scale channel metrics obtained by aggregating measured and predicted rays across all Rx locations. (a) Delay mean (b) AZ AoA mean (c) EL AoA mean (d) Delay spread (e) AZ AoA spread (f) EL AoA spread.

Diffuse rays: Diffuse scattering, rather, was found to better approximate the prominent interactions with vehicles; indeed, the ensemble of vehicles could be viewed as clutter, generating rays with random properties to mimic the macro diffuse behavior. In fact, the calibrated parameters yielded stronger diffuse reflections from vehicles (*diffuse scaling factor* = 2.2), in part to compensate for deactivation of their specular reflections and diffractions. The foliage yielded weaker diffuse reflections (*diffuse scaling factor* = 0.4) and wider angle spreads ($\beta_S = 70^\circ$). The six large-scale channel metrics for calibrating the diffuse rays (mentioned earlier) were computed from the measured rays for each Rx location and subsequently aggregated across all Rx's in cumulative distribution functions (CDFs), displayed in Fig. 8. Analogous CDFs were computed for the predicted rays for the three calibration stages (initial, intermediate, final) to underscore the incremental benefit of each stage. In addition to CDFs, the mean measured and predicted metrics across all Rx's were reported in Table II, as well the mean absolute error between the two. As expected, the final calibration provided the best overall fit among all stages, especially for the delay spread (up to 15.3 ns better), AZ AoA spread (up to 9.3° better), and EL AoA spread (up to 0.9° better); however, because the metrics are interdependent, the final calibration was not best for *each* metric:

exceptions were for the delay mean (4.6 ns worse than initial) and AZ AoA mean (0.9° worse than initial).

The measured channel overall was found to have wide AZ angle spread, which narrowed with increasing Tx-Rx distance, and both positive (from foliage) and negative (from vehicles) EL angles for delays below 100 ns – faithfully reproduced by *Volcano*. In fact, when comparing Fig. 6(d) to Fig. 6(a), it is evident that the calibrated PADPs correlate well with the measured PADPs – both in terms of ray density and delay and angle spreads – thanks to the incorporation of diffuse scattering, most notably increasing the ray density and the EL angle spread. Indeed, the importance of diffuse scattering cannot be underestimated as it was found to account on average for 20% of the total measured power per Rx, whereas the specular rays only accounted for 5%;⁶ 75% was attributed to the direct ray and the power attributed to diffraction was less than 1%.

Finally, it was observed that *Volcano* well approximates the total number of channel rays – the majority of which are due to diffuse scattering – within the Tx-Rx distance of 55 m: there were only 5% more predicted rays on average. This

⁶In other scenarios, e.g. the urban-canyon environment, a higher percentage of specular power could be expected due to the waveguide effect.

TABLE II
LARGE-SCALE CHANNEL METRICS

Statistic	Measured	Predicted (at various calibration stages)		
		Initial	Intermediate	Final
Delay mean	132.4 ns	136.5 ns	122.3 ns	123.7 ns
Error vs. measured	—	4.1 ns	10.1 ns	8.7 ns
Delay spread	50.3 ns	68.3 ns	46.8 ns	47.6 ns
Error vs. measured	—	18.0 ns	3.5 ns	2.7 ns
AZ AoA mean	172.1°	175.7°	176.2°	176.6°
Error vs. measured	—	3.6°	4.1°	4.5°
AZ AoA spread	28.1°	29.5°	17.5°	26.8°
Error vs. measured	—	1.4°	10.6°	1.3°
EL AoA mean	2.1°	1.9°	3.1°	1.9°
Error vs. measured	—	0.2°	1.0°	0.2°
EL AoA spread	2.5°	1.4°	3.2°	2.7°
Error vs. measured	—	1.1°	1.7°	0.2°

number, however, was underestimated by 16% beyond 55 m; at such long distance, the unpredicted rays likely corresponded to second-order diffusion or to a combination of specular and scattering interactions. Prediction accuracy would be enhanced by incorporating higher-order diffuse rays. It would also be enhanced, at the expense of much longer computation times, by GIS database with resolution as high as 10 cm (provided through LiDAR⁷ [72]), in particular to more precisely represent the intricacies of building façades, such as around metallic interaction points such as door and window frames and sills, as well as ambient objects that create blockage, such as light posts and foliage.

VI. CONCLUSION

In this paper, we presented a novel methodology to calibrate our *Volcano* ray-tracing engine against high-resolution directional measurements. The average error in the measured properties of the direct path was 1.2 dB in path gain, 0.55 ns in delay, 2.8° in AZ AoA, and 1.3° in EL AoA. The extensive measurement campaign consisted of 488 channel acquisitions collected at 28 GHz in an urban environment. The calibration methodology was based on minimizing the fit error between measured and predicted rays – mapped to each other individually – in their four-dimensional property domain, as well as in the space domain by tracking rays as the receiver traversed the environment. This enabled the calibration of object-specific models for diffuse scattering – namely distinct models for building, vehicles, and foliage – whose parameters were provided. The calibrated ray-tracer was able to faithfully reproduce the measurements, in terms of the properties of specular rays as well as in terms of the RMS delay and angle spreads generated by the diffuse rays: the average error in the delay, AZ AoA, and EL AoA spreads between the measured and predicted rays was 2.7 ns, 1.3°, and 0.2° respectively. Our chief finding was that, while most papers on millimeter-wave ray-tracing do not even

⁷To our knowledge, it was not available from any GIS vendors for the specific area in our study.

consider it, diffuse scattering accounted for 20% of the total received power, whereas diffraction accounted for less than 1%.

REFERENCES

- [1] Y. Okumura, “Field strength and its variability in VHF and UHF land-mobile radio service,” *Rev. Electr. Commun. Lab.*, vol. 16, pp. 825–873, 1968.
- [2] M. S. Mollel and M. Kisangiri, “An overview of various propagation model for mobile communication,” in *Proc. 2nd Pan Afr. Int. Conf. Sci., Comput. Telecommun. (PACT 2014)*, Arusha, Jul. 2014, pp. 148–153.
- [3] D. Sharma, P. K. Sharma, V. Gupta, and R. K. Singh, “A survey on path loss models used in wireless communication system design,” *Int. J. Recent Trends Eng. Technol.*, vol. 3, no. 2, pp. 115–118, May 2010.
- [4] G. Sati and S. Singh, “Comparison of various outdoor propagation models with empirical data collection using tems 10.0. 5 for DIT University, Dehradun,” *Int. J. Comput. Appl.*, vol. 97, no. 10, pp. 9–13, Jul. 2014.
- [5] N. Faruk, Y. A. Adediran, and A. A. Ayeni, “Error bounds of empirical path loss models at VHF/UHF bands in Kwarra state, Nigeria,” in *Proc. Eurocon 2013*, Zagreb, Jul. 2013, pp. 602–607.
- [6] J. Baumgarten, K. L. Chee, A. Hecker, T. Kürner, M. Braun, and P. Zah, “Performance of prediction models in suburban/rural residential areas at 860, 2300 and 3500 MHz,” in *Proc. 6th Eur. Conf. Antennas Propag. (EUCAP)*, Prague, Mar. 2012, pp. 1412–1416.
- [7] V. S. Abhayawardhana, I. J. Wassell, D. Crosby, M. P. Sellars, and M. G. Brown, “Comparison of empirical propagation path loss models for fixed wireless access systems,” in *Proc. IEEE 61st Veh. Technol. Conf.*, Stockholm, May 2005, pp. 73–77.
- [8] B. Y. Hancı and I. H. Cavdar, “Mobile radio propagation measurements and tuning the path loss model in urban areas at GSM-900 band in Istanbul-Turkey,” in *Proc. IEEE 60th Veh. Technol. Conf., 2004. VTC2004-Fall. 2004*, Los Angeles, CA, Sep. 2004, pp. 139–143.
- [9] J. V. Rodriguez *et al.*, “Comparison of various urban radiowave propagation models with measurements,” *IEEE Antennas Wireless Propag. Lett.*, vol. 8, pp. 977–980, Aug. 2009.
- [10] A. Mousa, Y. Dama, M. Najjar, and B. Alsayeh, “Optimizing outdoor propagation model based on measurements for multiple RF cell,” *Int. J. Comput. Appl.*, vol. 60, no. 5, pp. 5–10, Jan. 2012.
- [11] J. Milanovic, S. Rimac-Drlje, and K. Bejuk, “Comparison of propagation models accuracy for WiMAX on 3.5 GHz,” in *Proc. 14th IEEE Int. Conf. Electron., Circuits Syst.*, Marrakech, Dec. 2007, pp. 111–114.
- [12] M. N. Abdallah *et al.*, “Further validation of an electromagnetic macro model for analysis of propagation path loss in cellular networks using measured driving-test data,” *IEEE Antennas Propag. Mag.*, vol. 56, no. 4, pp. 108–129, Aug. 2014.
- [13] M. K. Samimi, T. S. Rappaport, and G. R. MacCartney, “Probabilistic omnidirectional path loss models for millimeter-wave outdoor communications,” *IEEE Wireless Commun. Lett.*, vol. 4, no. 4, pp. 357–360, Aug. 2015.
- [14] T. S. Rappaport *et al.*, “Wideband millimeter-wave propagation measurements and channel models for future wireless communication system design,” *IEEE Trans. Commun.*, vol. 63, no. 9, pp. 3029–3056, Sep. 2015.
- [15] O. H. Koymen *et al.*, “Indoor mm-Wave channel measurements: Comparative study of 2.9 GHz and 29 GHz,” in *Proc. IEEE Glob. Commun. Conf. (GLOBECOM)*, 2015, pp. 1–6.
- [16] I. Rodriguez *et al.*, “An empirical outdoor-to-indoor path loss model from below 6 GHz to cm-wave frequency bands,” *IEEE Antennas Wireless Propag. Lett.*, vol. 16, pp. 1329–1332, Dec. 2016.
- [17] F. Huang *et al.*, “Propagation characteristics of indoor radio channel from 3.5 GHz to 28 GHz,” in *Proc. IEEE 84th Veh. Technol. Conf. (VTC-Fall)*, Montreal, QC, Canada, 2016, pp. 1–5.
- [18] C. L. Cheng, S. Kim, and A. Zajić, “Comparison of path loss models for indoor 30 GHz, 140 GHz, and 300 GHz channels,” in *Proc. 11th Eur. Conf. Antennas Propag. (EUCAP)*, Paris, 2017, pp. 1–5.
- [19] A. Bamba, F. Mani, and d'E Raffaele, “A comparison of indoor channel properties in V and E bands,” in *Proc. 11th Eur. Conf. Antennas Propag. (EUCAP)*, Paris, 2017, pp. 1–5.
- [20] P. Zhang, J. Li, H. Wang, H. Wang, and W. Hong, “Indoor small-scale spatiotemporal propagation characteristics at multiple millimeter-wave bands,” *IEEE Antennas Wireless Propag. Lett.*, vol. 17, no. 12, pp. 2250–2254, Sep. 2018.
- [21] F. Erden, O. Ozdemir, and I. Guvenc, “28 GHz mmWave channel measurements and modeling in a library environment,” in *Proc. IEEE Radio Wireless Symp. (RWS)*, San Antonio, TX, USA, 2020, pp. 1–4.

- [22] B. De Beelde *et al.*, "60 GHz path loss modelling inside ships," in *Proc. 14th Eur. Conf. Antennas Propag. (EuCAP)*, Copenhagen, Denmark, 2020, pp. 1–5.
- [23] D. Dupleich, R. Müller, M. Landmann, J. Luo, G. D. Galdo, and R. S. Thomä, "Multi-band characterization of propagation in industry scenarios," in *Proc. 14th Eur. Conf. Antennas Propag. (EuCAP)*, Copenhagen, Denmark, Mar. 2020, pp. 1–5.
- [24] J. Zhang, C. A. Gentile, and W. D. Garey, "On the cross-application of calibrated pathloss models using area features: Finding a way to determine similarity between areas," *IEEE Antennas Propag. Mag.*, vol. 62, no. 1, pp. 40–50, Feb. 2020.
- [25] S. G. Larew *et al.*, "Air interface design and ray tracing study for 5G millimeter wave communications," in *Proc. IEEE Globecom Workshops (GC Wkshps)*, Atlanta, GA, pp. 1–6, 2013.
- [26] C. Wang *et al.*, "Ray-tracing based performance evaluation of 5G mmWave massive MIMO in hotspots," in *Proc. Int. Symp. Antennas Propag. (ISAP)*, Okinawa, 2016, pp. 1–2.
- [27] D. Solomitckii *et al.*, "Characterization of mmWave channel properties at 28 and 60 GHz in factory automation deployments," in *Proc. IEEE Wireless Commun. Netw. Conf. (WCNC)*, Barcelona, 2018, pp. 1–6.
- [28] X. Lin *et al.*, "Angular spread characteristics in high-speed railway scenarios in millimeter-wave band," in *Proc. 12th Eur. Conf. Antennas Propag. (EuCAP 2018)*, London, 2018, pp. 1–5.
- [29] M. J. Kazemi, A. Abdipur, and A. Mohammadi, "Indoor propagation MIMO channel modeling in 60 GHz using SBR based 3D ray tracing technique," in *Proc. 2nd Conf. Millimeter-Wave Terahertz Technol. (MMWaTT, IEEE)*, Dec. 2012, pp. 25–28.
- [30] Q. Li *et al.*, "Validation of a geometry-based statistical mmWave channel model using simulation," in *Proc. IEEE 81st Veh. Technol. Conf. (VTC Spring)*, 2015, pp. 1–5.
- [31] B. Sun, J. Yang, D. He, L. Zhao, D. Li, and J. Kim, "Efficient geometry-based channel modeling for mmWave high-speed train communication," in *Proc. 12th Int. Symp. Antennas, Propag. EM Theory (ISAPE)*, Hangzhou, Dec. 2018, pp. 1–4.
- [32] S. Li *et al.*, "Simulation and modeling of millimeter-wave channel at 60 GHz in indoor environment for 5G wireless communication system," in *Proc. IEEE Int. Conf. Comput. Electromagn. (ICCEM)*, 2018, pp. 1–3.
- [33] S. Li *et al.*, "Millimeter-wave channel simulation and statistical channel model in the cross-corridor environment at 28 GHz for 5G wireless system," in *Proc. Int. Conf. Microw. Millimeter Wave Technol. (ICMMT)*, 2018, pp. 1–3.
- [34] S. A. Rao and N. Kumar, "Modeling and link budget estimation of directional mmWave outdoor environment for 5G," in *Proc. Eur. Conf. Netw. Commun. (EuCNC)*, Jun. 2019, pp. 106–111.
- [35] S. Hur *et al.*, "Proposal on millimeter-wave channel modeling for 5G cellular system," *IEEE J. Sel. Top. Signal Process.*, vol. 10, no. 3, pp. 454–469, Apr. 2016.
- [36] J. H. Lee, J. S. Choi, J. Y. Lee, and S. C. Kim, "Permittivity effect of building materials on 28 GHz mmWave channel using 3D ray tracing simulation," in *Proc. IEEE Glob. Commun. Conf.*, Singapore, Dec. 2017, pp. 1–6.
- [37] J. H. Lee, J. S. Choi, and S. C. Kim, "Cell coverage analysis of 28 GHz millimeter wave in urban microcell environment using 3-D ray tracing," *IEEE Trans. Antennas Propag.*, vol. 66, no. 3, pp. 1479–1487, Mar. 2018.
- [38] B. Kim, H. Kim, D. Choi, Y. Lee, W. Hong, and J. Park, "28 GHz propagation analysis for passive repeaters in NLOS channel environment," in *Proc. 9th Eur. Conf. Antennas Propag. (EuCAP)*, Apr. 2015, pp. 1–4.
- [39] X. Sun, Y. Liu, and S. Li, "Study on 60 GHz millimeter wave propagation characteristics inside a bus based on SBR/IM Method," in *Proc. Int. Conf. Microw. Millimeter Wave Technol. (ICMMT)*, Chengdu, 2018, pp. 1–3.
- [40] J. H. Lee, J. S. Choi, J. Y. Lee, and S. C. Kim, "28 GHz millimeter-wave channel models in urban microcell environment using three-dimensional ray tracing," *IEEE Antennas Wireless Propag. Lett.*, vol. 17, no. 3, pp. 426–429, Mar. 2018.
- [41] T. A. Thomas, H. C. Nguyen, G. R. MacCartney, and T. S. Rappaport, "3D mmWave channel model proposal," in *Proc. IEEE 80th Veh. Technol. Conf. (VTC2014-Fall)*, Sep. 2014, pp. 1–6.
- [42] H. C. Nguyen, G. R. MacCartney, T. Thomas, T. S. Rappaport, B. Vejlgaard, and P. Mogensen, "Evaluation of empirical ray-tracing model for an urban outdoor scenario at 73 GHz E-band," in *Proc. IEEE 80th Veh. Technol. Conf. (VTC2014-Fall)*, Sep. 2014, pp. 1–6.
- [43] A. Karstensen *et al.*, "Comparison of ray tracing simulations and channel measurements at mmWave bands for indoor scenarios," in *Proc. 10th Eur. Conf. Antennas Propag. (EuCAP)*, 2016, pp. 1–5.
- [44] A. Zhou *et al.*, "60 GHz channel measurements and ray tracing modeling in an indoor environment," in *Proc. 9th Int. Conf. Wireless Commun. Signal Process. (WCSP)*, Nanjing, 2017, pp. 1–6.
- [45] S. Wei, B. Ai, D. He, K. Guan, L. Wang, and Z. Zhong, "Calibration of simulator for millimeter-wave outdoor communications," in *Proc. IEEE Int. Symp. Antennas Propag. USNC/URSI Nat. Radio Sci. Meeting*, Jul. 2017, pp. 1907–1908.
- [46] T. Zhou, H. Li, R. Sun, Y. Wang, L. Liu, and C. Tao, "Simulation and analysis of propagation characteristics for tunnel train-ground communications at 1.4 and 40 GHz," *IEEE Access.*, vol. 7, pp. 105123–105131, Jul. 2019.
- [47] C. Zheng, Z. Xu, D. He, K. Guan, B. Ai, and J. M. García-Loygorri, "Millimeter-Wave channel measurement based calibration and analysis in metro," in *Proc. IEEE Int. Symp. Antennas Propag. USNC-URSI Radio Sci. Meeting*, Atlanta, GA, USA, Jul. 2019, pp. 1–2.
- [48] D. He *et al.*, "Channel measurement, simulation, and analysis for high-speed railway communications in 5G millimeter-wave band," *IEEE Trans. Intell. Transp. Syst.*, vol. 19, no. 10, pp. 3144–3158, Oct. 2017.
- [49] D. He *et al.*, "Influence analysis of typical objects in rural railway environments at 28 GHz," *IEEE Trans. Veh. Technol.*, vol. 68, no. 3, pp. 2066–2076, Mar. 2018.
- [50] L. Wang *et al.*, "Vehicle-to-infrastructure channel characterization in urban environment at 28 GHz," *China Commun.*, vol. 16, no. 2, pp. 36–48, 2019.
- [51] A. Maltsev *et al.*, "Quasi-deterministic approach to mmwave channel modeling in a non-stationary environment," in *Proc. IEEE Globecom Workshops (GC Wkshps)*, Austin, TX, USA, Dec. 2014, pp. 966–971.
- [52] B. Ai *et al.*, "On indoor millimeter wave massive MIMO channels: Measurement and simulation," *IEEE J. Sel. Areas Commun.*, vol. 35, no. 7, pp. 1678–1690, Jul. 2017.
- [53] K. Guan *et al.*, "Towards realistic high-speed train channels at 5G millimeter-wave band—Part I: Paradigm, significance analysis, and scenario reconstruction," *IEEE Trans. Veh. Technol.*, vol. 67, no. 10, pp. 9112–9128, Oct. 2018.
- [54] J. Senic *et al.*, "Analysis of E-band path loss and propagation mechanisms in the indoor environment," *IEEE Trans. Antennas Propag.*, vol. 65, no. 12, pp. 6562–6573, Dec. 2017.
- [55] C. Gentile *et al.*, "Quasi-deterministic channel model parameters for a data center at 60 GHz," *IEEE Antennas Wireless Propag. Lett.*, vol. 17, no. 5, pp. 808–812, May 2018.
- [56] C. Lai *et al.*, "Methodology for multipath-component tracking in millimeter-wave channel modeling," *IEEE Trans. Antennas Propag.*, vol. 67, no. 3, pp. 1826–1836, Mar. 2018.
- [57] V. Degli-Esposti, F. Fuschini, E. M. Vitucci, and G. Falciasecca, "Measurements and modelling of scattering from buildings," *IEEE Trans. Antennas Propag.*, vol. 55, no. 1, pp. 143–153, Jan. 2007.
- [58] Y. Corre and Y. Lostanlen, "Three-dimensional urban EM wave propagation model for radio network planning and optimization over large areas," *IEEE Trans. Veh. Technol.*, vol. 58, no. 7, pp. 3112–3123, Sep. 2009.
- [59] P. B. Papazian *et al.*, "A radio channel sounder for mobile millimeter-wave communications: System implementation and measurement assessment," *IEEE Trans. Microw. Theory Techn.*, vol. 64, no. 9, pp. 2924–2932, Sep. 2016.
- [60] P. B. Papazian *et al.*, "Calibration of millimeter-wave channel sounders for super-resolution multipath component extraction," in *Proc. 10th Eur. Conf. Antennas Propag. (EuCAP)*, 2016, pp. 1–5.
- [61] R. Sun *et al.*, "Design and calibration of a double-directional 60 GHz channel sounder for multipath component tracking," in *Proc. 11th Eur. Conf. Antennas Propag. (EUCAP)*, 2017, pp. 1–5.
- [62] S. R. Saunders, *Antennas and Propagation for Wireless Communication Systems*, First Edition. Hoboken, NJ, USA: Wiley-Blackwell, 1999.
- [63] R. G. Kouyoumjian and P. H. Pathak, "A uniform geometrical theory of diffraction for an edge in a perfectly conducting surface," *Proc. IEEE*, vol. 62, no. 11, pp. 1448–1461, Nov. 1974.
- [64] G. Gougeon, Y. Lostanlen, and L. Maviel, "Coupling a deterministic propagation model with diffuse scattering and urban furniture for small cells," in *Proc. 5th Eur. Conf. Antennas Propag. (EuCAP)*, Rome, Apr. 2011, pp. 1–5.
- [65] F. T. Ulaby *et al.*, "Millimeter-wave bistatic scattering from ground and vegetation targets," *IEEE Trans. Geosci. Remote Sens.*, vol. 26, no. 3, pp. 229–243, May 1988.
- [66] F. K. Schwering, K. Felix, E. J. Violette, and R. H. Espeland, "Millimeter-wave propagation in vegetation: Experiments and theory," *IEEE Trans. Geosci. Remote Sens.*, vol. 26, no. 3, pp. 355–367, May 1988.
- [67] OpenStreetMap Project, 2020. [Online]. Available: www.openstreetmap.org

- [68] Google Earth, 2020. [Online]. Available: <https://earth.google.com/web/>
- [69] ITU, Recommendation ITU-R P.2040-1, "Effects of building materials and structures on radiowave propagation above about 100 MHz," Jul. 2015.
- [70] ITU, Recommendation ITU-R P.833-9, "Attenuation in vegetation," Sep. 2016.
- [71] ITU, Recommendation ITU-R P.676-12, "Attenuation by atmospheric gases and related effects," Aug. 2019.
- [72] M. Z. Aslam, Y. Corre, J. Belschner, G. S. Arockiaraj, and M. Jäger, "Analysis of 60-GHz in-street backhaul channel measurements and LiDAR ray-based simulations," in *Proc. 15th Eur. Conf. Antennas Propag. (EuCAP)*, Copenhagen, Denmark, Mar. 2020, pp. 1–5.



Romain Charbonnier received the Engineering degree and the M.Sc. degree in telecommunications from INSA, Rennes, France. He joined Siradel, France, in 2006, as a Research Engineer. He developed a special expertise in the simulation of the radio-wave propagation (from sub-6GHz to millimeter-wave frequencies) and measurement-based calibration. He is elaborating software solutions for operational 5G network planning.



Chiehping Lai received the M.S. and Ph.D. degrees in electrical engineering from the Pennsylvania State University, State College, PA, USA. He is currently a Computer Engineer with NIST Communications Technology Laboratory, Gaithersburg, MD, USA. His research interests include mmWave systems, tracking algorithms, and data processing.



Thierry Tenoux received the Ph.D. degree in signal processing and telecommunication from the University of Rennes I, Rennes, France, in 1991. He was a Postdoctoral Researcher working on SAR polarimetric properties with the Laval University, Québec, QC, Canada. Since 1996, he has been a Research Radio Engineer with Siradel, Saint-Grégoire, France, with senior expertise on deterministic modeling of the radio propagation (5G, IRS) and depolarization effects.



Derek Caudill received the B.S. degree in electrical engineering and the M.S. degree in electrical and computer engineering from the University of Massachusetts Amherst, Amherst, MA, USA, in 2016 and 2017, respectively. As a researcher within the Communications Technology Laboratory, NIST, he supports the data acquisition efforts of mmWave channel model measurements and the systems that such measurements depend on.



Grégory Gougeon received the Engineering degree from INSA, Rennes, France, in 2001. Since then, he has evolved as an expert in outdoor and indoor radio-wave propagation and network design techniques with Siradel, Saint-Grégoire, France. He was involved in various French and European research projects aiming at the upgrade of deterministic channel models to the needs of new wireless technologies.



Jelena Senic received the B.S. and M.S. degrees in electrical engineering from the School of Electrical Engineering, University of Belgrade, Belgrade, Serbia, in 2009 and 2010, respectively. Since 2015, she has been a Guest Researcher with NIST, Gaithersburg, MD, USA. Her current research interests include millimeter-wave communications, measurements of signal propagation, and channel modeling for 5G. The team in which she works received the Best Measurement Paper Award at the 2017 European Conference on Antennas and Propagation.



Camillo Gentile (Member, IEEE) received the Ph.D. degree in electrical engineering from Pennsylvania State University, State College, PA, USA, in 2001, with a dissertation on computer vision and artificial intelligence. He joined the National Institute of Standards and Technology, Gaithersburg, MD, USA, in 2001, and is currently a Project Leader with the Wireless Networks Division, Communications Technology Laboratory. He has authored more than 80 peer-reviewed journal and conference papers, a book on geolocation techniques, and a book on millimeter-wave channel modeling. His current interests include channel modeling and physical-layer modeling for 5G communications systems.



Yoann Corre (Member, IEEE) received the Engineering degree from INSA, Rennes, France, and the M.Sc. degree from UCL, London, U.K., in 1999. He is currently a Wireless CTO with Siradel, Saint-Grégoire, France. At Siradel since 2000, he has been working as a Research Engineer on radio-wave propagation modelling (ray-tracing). He is currently leading the research activities on the wireless network simulation and design (cellular, WLAN, backhaul networks, etc.).



Jack Chuang received the Ph.D. degree in 2008. He was a Graduate Research Assistant with the Communications and Space Sciences Laboratory (CSSL), Pennsylvania State University, State College, PA, USA. Then, he was with BAE Systems in electronic warfare and with Cisco Systems in spectrum sharing. He is currently with NIST Communication Technology Laboratory, Gaithersburg, MD, USA, developing 5G mmWave channel sounders.



Nada Golmie (Senior Member, IEEE) received the Ph.D. degree in computer science from the University of Maryland, College Park, MD, USA. She is currently the Chief of the Wireless Networks Division, Communications Technology Laboratory, National Institute of Standards and Technology, Gaithersburg, MD. Her research in media access control and protocols for wireless networks led to more 100 technical papers presented at professional conferences and journals. She is a Co-Chair for the 5G mmWave Channel Model Alliance.